GT2019-91050

SYSTEMATIC EXPERIMENTAL EVALUATIONS AIMED AT OPTIMIZING THE GEOMETRY OF AXIAL CASING GROOVE IN A COMPRESSOR

Huang Chen
Johns Hopkins University
Department of Mechanical
Engineering
Baltimore, MD, USA

Subhra Shankha Koley
Johns Hopkins University
Department of Mechanical
Engineering
Baltimore, MD, USA

Yuanchao Li
Johns Hopkins University
Department of Mechanical
Engineering
Baltimore, MD, USA

Joseph Katz
Johns Hopkins University
Department of Mechanical
Engineering
Baltimore, MD, USA

ABSTRACT

Performance and flow measurements are carried out to investigate the impact of varying the geometry of axial casing grooves on the stall margin and efficiency of an axial turbomachine. Prior studies have shown that skewed semi-circular grooves installed near the blade leading edge (LE) have multiple effects on the flow structure, including ingestion of the tip leakage vortex (TLV), suppression of backflow vortices, and periodic variations of flow angle. To determine which of these phenomena is a key contributor, the present study examines the impact of several grooves, all with the same inlet geometry, but with outlets aimed at different directions. The "U" grooves that have circumferential exits aimed against the direction of blade rotation achieve the highest stall margin improvement of well above 60% but cause a 2.0% efficiency loss near the best efficiency point (BEP). The "S" grooves, which have exits aimed with the blade rotation, achieve a relatively moderate stall margin improvement of 36%, but they do not reduce the BEP efficiency. Other grooves, which are aligned with and against the flow direction at the exit from upstream inlet guide vanes, achieve lower improvements. These trends suggest that causing high periodic variations in flow angle around the blade leading edge is particularly effective in extending the stall margin, but also reduces the peak efficiency. In contrast, maintaining low flow angles near the LE achieves more moderate improvement in stall margin, without the maximum efficiency loss. Hence, of the geometries tested, the S grooves appear to have the best overall impact on the machine performance. Velocity measurements and flow visualizations are performed in an axial plane located downstream of the grooves, near the trailing edge of the rotor.

Reduced efficiency or performance co-occurs with elevated circumferential velocity in the tip region, but differences in the axial blockage are subtle. Yet, near the BEP, the regions with reduced axial velocity, or even negative velocity between the TLV and the endwall, are wider behind the U grooves compared to the S grooves. The vorticity profiles also show that at low flow rates the TLV is ingested entirely by the grooves, in contrast to the best efficiency point, where a considerable fraction of the TLV rollup occurs downstream of the grooves.

INTRODUCTION

Instabilities leading to rotating stall and surge in axial turbomachines have been attributed to blockage resulting from interactions between the tip leakage flow and the main flow [1–3]. Consequently, a series of endwall casing treatment methods, such as axial and circumferential casing grooves [4–6], have successfully extended the stall margins. However, they all involve an efficiency penalty close to the best efficiency point (BEP) of the machine. The axial casing grooves (ACGs) slots typically achieve greater improvements in the stall margin than circumferential slots, but they also cause higher efficiency losses [7–12]. Some studies (Fujita and Takata [8]) even conclude that the stall margin improvement and efficiency losses are linked, namely the larger the stall margin improvement, the larger the penalty. However, a few studies have reported only minimal losses in transonic compressors, e.g., a penalty of 0.5% in experiments reported by Müller et al. [13]. Others studies involving Reynolds-averaged Naiver-Stokes simulations have reported that the efficiency loss

depends on the location of the ACGs [14,15]. They are small when the groove is located near the leading edge (LE) of the blade, e.g., 0.2% reported by Wilke and Kau [9], but increase to 4% when the groove is located above the center of the blade, while the associated stall margin gains remain similar [14,15]. In contrast, Beheshti et al. [16] claim that ACGs increase the peak efficiency and Houghton and Day [17] provide examples with very small efficiency penalties for a stall margin improvements of about 4.5%. For axial grooves, Smith and Cumpsty [10] determine that the stall margin improvement is associated with momentum exchange caused by the pumping of fluid into the slot and out of the slot [10,18,19] and by the additional flow-path between the pressure and suction sides of the blade [10]. The published literature [2] also shows that circumferentially inclined axial grooves are more effective than radial ones. However, more complex geometries involving channels linking different points in the passage to others located upstream have not shown substantial benefits over the simpler grooves [6]. Self-regulating casing treatment that maintains the flow in the groove at low flow rates to delay stall, but minimizes it at high flow rates have also been introduced [6]

For spike-induced stall [20], recent simulations [21] have shown that it is associated with spillage of the flow at the tip leading edge caused by either local flow separation or by the tip-leakage flow, the latter consistent with [22–24]. The existence of this spillage has also been inferred experimentally based on pressure and surface oil visualizations [25–28]. Detailed velocity measurements and flow visualizations aimed at characterizing the flow structures involved have been performed in the JHU refractive index matched facility using the blade geometries illustrated in Fig. 1 [29–33]. They confirm that the onset of stall is indeed associated with the tip leakage flow [34]. Specifically, a rotating stall develops as backflow vortices (BFVs) developing radially inboard from the TLV, at the interaction of region affected by the TLV with the main passage flow, extend diagonally upstream, from the mid-chord suction side (SS) of one blade to the pressure side (PS) or the leading edge of the next blade [34]. When these structures penetrate to the next passage, either through the tip gap or upstream of the LE, they trigger a similar phenomenon there, initiating a process that sustains itself. Experiments performed in several other axial turbomachines at varying flow conditions have shown that the formation of BFV is a persistent phenomenon. Additional information on the flow structure and turbulence in the same untreated machine are provided in [35,36].

The next series of experiments have evaluated the impact of axial casing grooves on the performance, efficiency, flow structure and turbulence in the tip region of the rotor passage as well as inside the casing grooves. Initially, we have selected the same semi-circular grooves discussed in Müller et al. [13], which is illustrated in figure 1b and is referred to in the rest of this paper as ACGs [37]. These semi-circular ACGs are skewed by 45° in the positive circumferential direction. The four grooves per rotor blade passage partially overlap with the rotor blade LE, and the rest extends upstream. The performance (pressure rise) and efficiency have been measured across the entire range of flow rates, from beyond the BEP to well within the stall conditions. The visualizations and velocity measurements have been performed both at prestall flow rate of the untreated machine, namely $\varphi=V_z/U_T=0.25$, where V_z is the flow rate divided by the through-flow area, and U_T is the tip speed [38], and close to the BEP conditions, $\varphi=0.35$ and 0.38 [37]. Consistent with previously reported trends, the ACGs reduce the stall flow rate by nearly 40% to $\varphi=0.15$ but cause a 2.4% reduction in efficiency at BEP. At the prestall flow rate, the ACGs cause several changes to the flow structure. First, periodic inflow into the grooves when the downstream end of the groove is aligned with the blade PS ingests the TLV, leaving very little trace of it when the next blade arrives. Second, the outflow from the grooves in the negative circumferential direction limits the formation of regions with high circumferential velocity gradients inboard from the TLV around the blade LE, preventing the formation of BFVs there. Third, the intermittent injection of negative circumferential velocity causes substantial periodic variations in the flow angle around the rotor blade LE, altering the blade loading. The extent of these variations is demonstrated in Fig. 2 for both flow rates. Hence, the co-occurrence of multiple phenomena prevents us from stating conclusively which flow phenomenon is the primary cause for the substantial increase in stall margin. The present paper is our first step in identifying their relative significance.
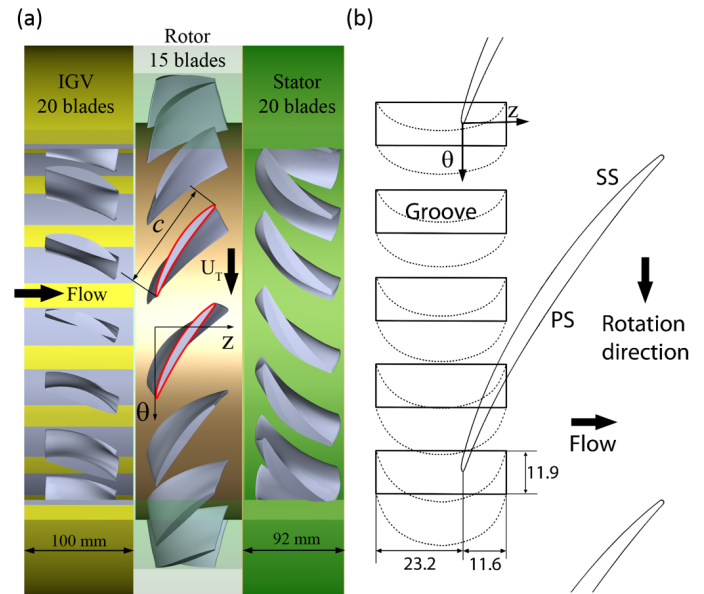
Figure 1: Configurations of (a) the one and a half stages compressor and (b) the original semi-circular ACGs (Müller et al.[13]). Dimensions are in mm.
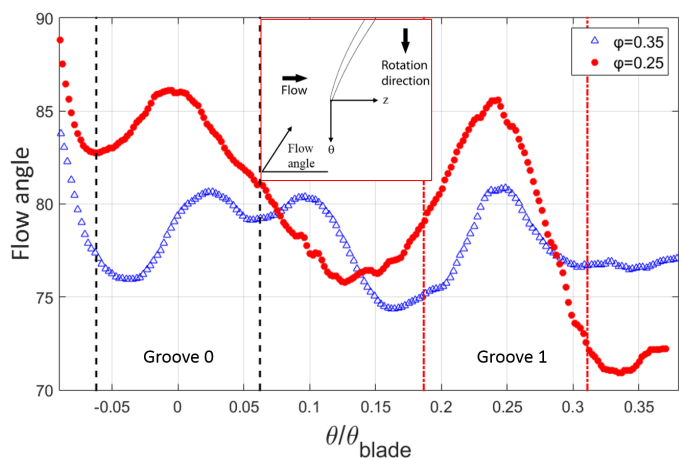
Figure 2: Flow angle, i.e., angle relative to the axial direction in the rotor reference frame, near the rotor blade LE for the original semi-circular ACGs. Dashed lines indicate the circumferential boundaries of the grooves.

At $\varphi=0.35$ and 0.38 Chen et al. [37] show that the periodic inflow into the groove decreases compared to those occurring at $\varphi=0.25$ (pre-stall of the untreated machine), but still ingest periodically the PS boundary layer and its vorticity. While being exposed to the blade SS, the backward tip leakage flow separates and forms a counter-rotating vortex at the downstream corner of the groove. At $\varphi=0.25$, this corner vortex along with TLV fragments are circulated in the grooves and become scrambled. In contrast, at $\varphi=0.35$ or 0.38, most of the TLV remain in the passage and is strong enough to entrain the corners vortex. Interactions between these structures create a broad area with secondary flows and elevated turbulence level over the entire tip region, presumably contributing to the reduced performance near the BEP.

As an essential fundamental step in elucidating the stall-suppression mechanisms, the primary objective of this paper is to determine which of the ACGs effects is the primary contributor to stall suppression. Included are the intermittent suction of the TLV into the groove, elimination of the radial gradients in circumferential velocity and BFVs, and the periodic modulation of the flow angle near the blade LE. To achieve this goal, we have designed a series of grooves, all of them having the same inlet (downstream end) geometry, but they have outlets aimed in different directions. Hence, the periodic suction of the TLV when the blade PS is exposed to the entrance to the groove is expected to occur in all of them. However, since their exits are aimed at different directions, they presumably have different effects on the distributions of circumferential velocity near the blade LE, and accordingly, different periodic variations flow in flow angle. The groove geometries are described in the following chapter. Performance and efficiency plots introduced subsequently show substantial variations in the levels of stall margin extensions and efficiency losses at high flow rates. In some of the cases, we have achieved considerable stall suppression without efficiency loss

at high flow rates, making them very attractive options for follow-up studies. The last part of the results compares the flow in the passage downstream of the grooves, close to the trailing edge of the rotor for two extreme cases, namely one that is extremely effective in suppressing stall, but causes efficiency loss, and the above-mentioned case with milder (but still substantial) stall suppression, but without efficiency loss.

**FACILITY AND GROOVE GEOMETRIES**

The test facility and the three-blade-rows axial compressor (Figure 1a) has been described in previous publications [31,34,38,39]. A summary of relevant geometric scales is provided in Table 1. The blades have the same profiles as those of the first three rows of the Low-Speed Axial Compressor (LSAC) in NASA Glenn, but the span has been reduced to accommodate operation using acrylic blades in a liquid. The fluid in the JHU refractive index matched facility, a concentrated aqueous solution of sodium iodide in water has the same refractive index as the blades, 1.49, accommodating velocity measurements and flow visualization at any point. However, due to cost considerations and the number of grooves involved, the presently used groove-containing rings that surround the leading edge of the rotor are not transparent, preventing us from performing velocity measurements inside the grooves or around the blade leading edge. These rings are made using rapid prototyping. However, we can still perform velocity measurements within the rotor passage downstream of the grooves to determine their impact on the flow structure near the rotor blade trailing edge. Based on the present conclusions, in a follow-up study, we plan to manufacture fully accessible grooves for two of the present cases and investigate the flow within and around them in greater detail.

Table 1 Stage relevant geometrical parameters

Casing diameter (D) (mm)	457.2
Hub radius (r_{hub}) (mm)	182.9
Rotor passage height (L) (mm)	45.7
Rotor diameter (D_R) (mm)	453.6
Rotor blade chord (c) (mm)	102.6
Rotor blade span (H) (mm)	43.9
Rotor blade stagger angle (γ) (deg)	58.6
Rotor blade axial chord (c_A) (mm)	53.5
Measured tip clearance (h) (mm)	1.8 (0.0175c or 0.041H)
Axial casing groove diameter (mm)	34.8
Groove skew angle (deg)	45
Total number of grooves	60
Shaft speed (Ω) (rad s^{-1}) {RPM}	50.27 {480}
Rotor blade tip speed (U_T) (m s^{-1})	11.47
Reynolds number ($U_T c / \nu$)	1.07×10^6
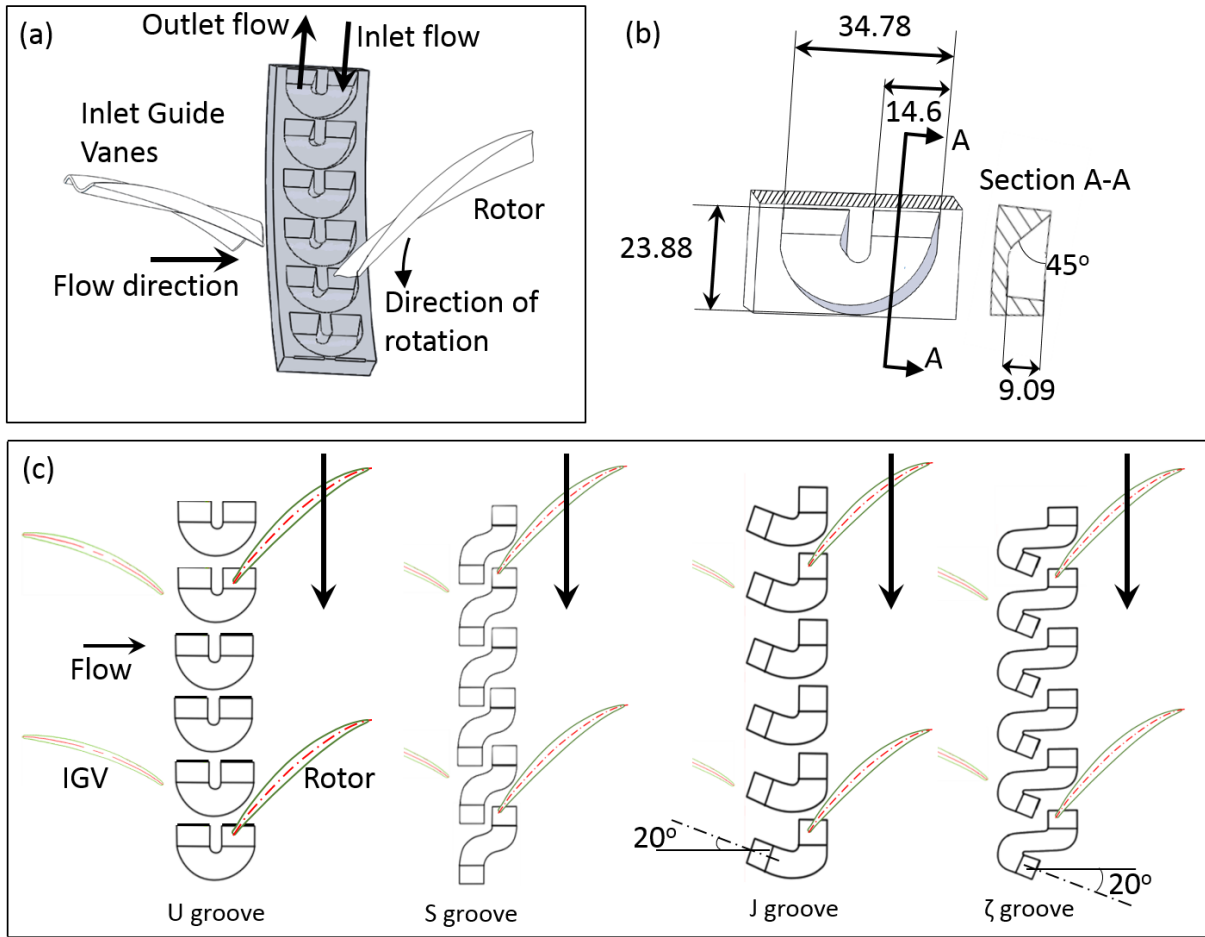
Figure 3: The geometry of the present casing grooves. (a) The location and orientation of the U grooves relative to the rotor and IGV blades; (b) Dimensions of the U groove in mm; (c) the shapes and orientation of the grooves.
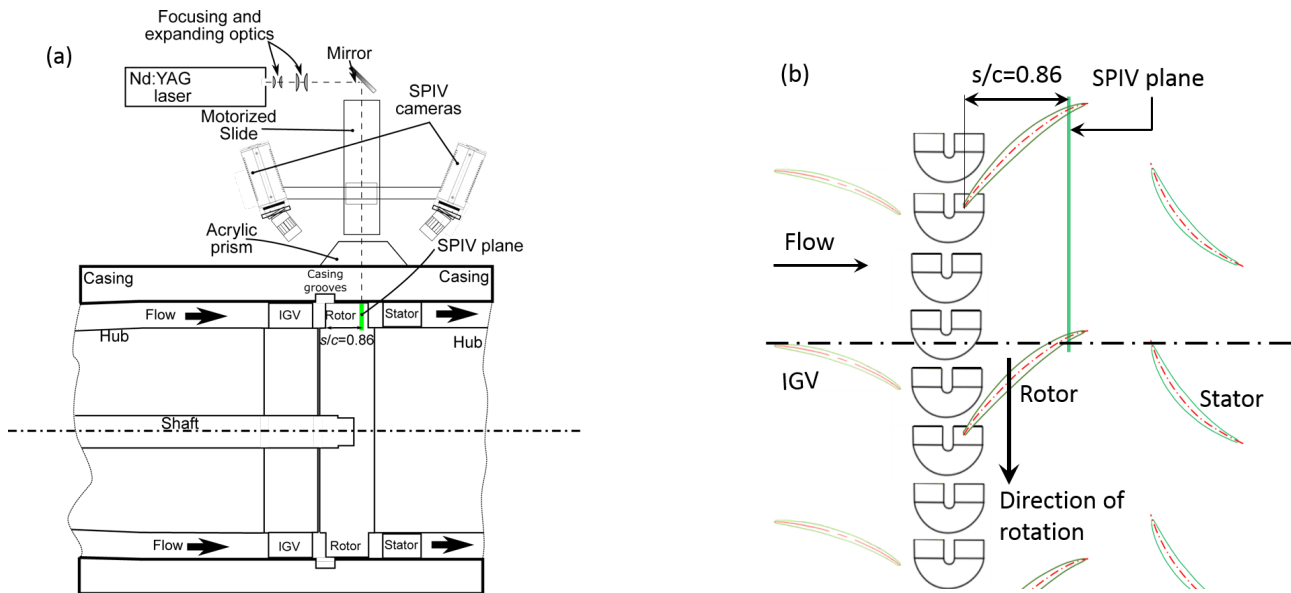
Figure 4: Experimental setups for SPIV measurements in an axial (r, θ) plane near the trailing edge of the rotor: (a) side view, and (b) top view.

Four of the grooves, the focus of the present paper, are illustrated in Figure 3. They are labeled as "U," "S," "J," and "ζ" grooves. In all cases, as illustrated for the U groove in Figure 3a, the downstream one-third of the groove overlaps with the blade leading edge, and the rest extends upstream and occupies most of the space between the IGV and the rotor. This axial positioning and overlap fraction are consistent with those of the original skewed semi-circular ACG (Fig. 1). The grooves are evenly spaced circumferentially, and there are four grooves per blade passage, also in agreement with the semi-circular ACG. They have the same inlet dimensions and shapes, but different outflow orientations. The inlet to each groove has a width of 14.76 mm (8.2 times the tip gap) consists of a 45° and 9.08 mm deep ramp aligned in the positive circumferential direction. The shape of this ramp has been selected to resemble that of the entrance to the original ACGs. The outlets also have a 45° ramp. The exit from the U groove is aligned in the negative circumferential direction, and consequently, is expected to a general orientation of the exit flow resembling that of the semi-circular ACG. In contrast, the S groove directs the outflow in the positive circumferential direction. In the J groove, the outflow is directed against the outflow from the inlet guide vane (IGV), and in the ζ groove, the outflow is directed with the outflow from the IGV grooves. All of the grooves are open, i.e. they basically consist of open channels with ramped ends. We have also tested (not shown) "closed" grooves, where only the ramps are open, and the rest of the channel is closed. Additional information, including comments on results obtained for other open grooves, is provided later.

EXPERIMENTAL SETUPS

During all tests, the rotor speed is fixed at 480 RPM, resulting in a Reynolds number of 1.07×10^6 based on the rotor blade chord length. The facility is equipped with an auxiliary pump that allows us to operate at higher flow rates. To achieve a lower flow rate, the resistance of the loop is increased by adding different mesh blocks in the return line. The driving motor input power is monitored by a manufacturer pre-calibrated strain gauge torque meter (SensorData® T261-STD-A) whose uncertainty is around 0.1%. During efficiency calculation, the torque required to overcome the resistance of the bearing and shaft, measured by running the rotor hub without blades, has been subtracted. The volumetric flow rate is calculated by the integration of the velocity profile which is obtained by traversing a Pitot tube radially in the return line, while the pressure rise is measured by a differential pressure transducer connected to pressure ports upstream of the IGV and downstream of the stator. Each data point in the performance curve is the average of 200,000 data points obtained during a 60s interval by a 3.3 kHz data acquisition device. The experimental uncertainty associated with the measured head rise, flow rate, and efficiency is around 1.2%, 1.7%, and 2.2%, respectively, accounting all contributing factors including equipment uncertainties and standard deviations of the

transducer signals. More detailed information about the uncertainties is described in Chen et al.[37].

SPIV measurements (Fig. 4a) are conducted at two flow rates, $\varphi = 0.25$ and 0.38, for S and U grooves in a axial plane (r, θ) at 86% (Fig. 4b) of the rotor chord away from the leading edge (LE) (i.e., $s/c = 0.86$, where s is the chordwise coordinate whose origin is at LE.) The imaging system is synchronized by an encoder mounted on the rotor shaft, allowing us to record data at the same blade phase. The flow field is illuminated by a 1mm thick laser sheet expanded from a dual pulse, 200mJ/pulse Nd:YAG laser beam. The spherical glass particles are silver coated with a mean diameter and density of 13μm and 1.6g/mm^2, respectively. Since the cross-plane velocity component is dominant, delays between exposures have been set at 60μs for $\varphi = 0.25$ and 40μs for $\varphi = 0.38$, ensuring enough particle displacements in the images (~12-20px) while retaining most of the particles in the laser sheet during two exposures. Shown in Fig. 4a, the particle images in the 111.3×134.8 mm^2 field of view are recorded by two Imperx B6640 CCD cameras (6600×4400 px^2), covering an entire rotor passage from the casing wall to the hub (Fig. 4b). The resulting vector spacing by using 50% overlap with 24×24 px^2 final interrogation windows is 0.283mm. The imaging system is carefully calibrated using a two-step process described by Wieneke [40]. The first step involves traversing the entire system up as a whole to image an axially translating dotted calibration target in a box filled with the same solution, mimicking the optical setup in the actual measurement plane. The second step is done by correlating particle images recorded in the laser sheet after lowering the imaging system back to its original position. The uncertainties associated with the SPIV measurement of instantaneous flow fields are around 0.4%~0.8%U_T based on our prior studies [30], given there are enough particles (>=5) in the interrogation windows. The uncertainties of the averaged data of 800-1000 samples in current experiments should be much lower. The ensemble-averaged velocities are presented in a cylindrical coordinate system (r, θ, z) centered at rotor hub. The corresponding components in the lab reference frame, (U_r, U_θ, U_z), are transformed from the Cartesian components obtained from the SPIV measurements. The axial vorticity ω_Z is calculated directly from the SPIV results in the Cartesian system since ω_Z is invariant in the two coordinate systems.

To obtain qualitative visualizations of the vortical structures, the mean pressure of the loop is lowered to induce cavitation in vortices. The flow field is illumined from the side by halogen lamps and cavitation images are recorded by a high-speed camera at 5760fps. Since the grooves used in the current study are non-transparent and covering the LE portion of the blade, the images are obtained from a shallow angle looking upstream, picking up most of the structures downstream of the groove. It is worth noting that during SPIV measurement, the mean pressure in the loop is increased to suppress all forms of cavitation.

RESULTS AND DISCUSSIONS

Performance and Efficiency Curves

Plots of the static-to-static head rise coefficient, defined as $\psi_{SS}=(P_{exit}-P_{in})/0.5\rho U_T^2$, where $P_{exit}-P_{in}$ represents the pressure rise across the entire machine, are presented in Figs. 5a and b. The former covers the entire range of flow coefficients expressed as $\varphi=V_Z/U_T$, and the latter focuses on the high flow rate range. The efficiency of the machine (η) for the different casing grooves is presented in Figs. 5c and d, with the latter again highlighting the high flow rate range. Here, $\eta=(P_{exit}-P_{in})Q/T\Omega$, where Q is the volumetric flow rate and T is the torque measured by the torque meter after subtracting the effects of bearings (torque measured when the blades are removed). The uncertainty in the measurements is illustrated by error bars for one of the data points. The plots contain results for the original untreated endwall, the semi-circular ACG, as well as for the open U, S, J and ζ grooves. As is evident and discussed before [34], the stall onset for the smooth endwall occurs at $\varphi=0.25$. Installing the original ACG increases the magnitude of ψ_{SS} at $\varphi=0.25$, shifts the stall point to $\varphi<0.15$. However, as is particularly evident from Figs. 5b & d, these ACGs cause a reduction in ψ_{SS} at $\varphi>0.36$, and a decrease in efficiency at $\varphi>0.35$. The peak efficiency decreases by 2.5% and shifts to a lower flow rate.

The U grooves extend the stall margin even further, to $\varphi=0.1$, representing a striking 60% improvement compared to the untreated endwall. At $\varphi=0.1$, the head coefficient decreases abruptly. On the other side of the performance curve, the values of ψ_{SS} match those of the untreated endwall at $\varphi=0.38$, and fall slightly below them at higher flow rates. However, at $\varphi>0.36$ the efficiency falls well below that of the smooth endwall, and do not differ significantly from those of the semi-circular grooves. The S grooves extend the stall margin to $\varphi=0.16$, representing a substantial 36% improvement, but not to the same extent as the ACGs and the U grooves. The head coefficient matches those associated with the other grooves down to $\varphi=0.25$ but then plateaus before decreasing at $\varphi<0.16$. At high flow rates ($\varphi>0.37$) the magnitudes of ψ_{SS} are marginally higher (within the uncertainty range) than those of the smooth endwall. However, most importantly, the S grooves do not cause an efficiency penalty and maintain the same (even marginally higher) peak efficiency of slightly below 85% at the same flow rate as the untreated endwall. As the error bars in Figure 5c indicate, the efficiency penalty caused by the semi-circular ACGs and U grooves at high flow rates, in contrast to the S grooves, which maintain the original efficiency, exceed the uncertainty in the present measurements. Furthermore, to ensure that results are repeatable, several of the tests have been repeated at a different time, and both results, which show consistent trends, are included in Fig. 5.

As for the ζ grooves, which are aligned with the outflow from the IGV, they have limited effect on the stall margin,

reducing the stall flow coefficient only from 0.25 to 0.23. At high flow rates, they maintain high head coefficients matching those of the S groove. The associated efficiencies are only slightly lower than those of the S groove. The J groove, whose exit is aligned in the opposite direction to outflow from the IGV achieve a higher improvement to the stall margin, reducing it from 0.25 to 0.18. However, at high flow rates, the J grooves cause an efficiency loss matching those of the semi-circular ACGs and the U grooves.

In summary, the U grooves achieve the highest stall margin improvements but cause the familiar efficiency loss at high flow rates. In contrast, the S grooves still achieve a substantial stall margin improvement, but not to the same extent as the U grooves. However, they do not cause an efficiency penalty at high flow rates. Hence, of the geometries tested, the S grooves appear to have the best overall impact on the machine performance. Since both grooves have the same inlet geometry, it appears that the aligning the outflow in the negative circumferential direction achieves better stall margin improvement, presumably owing to the associated larger periodic variations in flow angle near the rotor blade leading edge. Near BEP, these flow angle oscillations appear to contribute to a reduction in machine efficiency. These postulates will be tested in future studies.

Before continuing, as noted before, we have also tested grooves that are not included in Figure 5. First, a U groove with a closed channel except for the inlet and exit ramps maintains the same elevated values of ψ_{SS} as the other grooves down to $\varphi=0.25$ but then stalls abruptly. Thus, it increases the blade loading up to the pre-stall conditions but does not extend the stall margin. Near BEP, the efficiency falls slightly below that of the untreated wall and is clearly higher than that of the open U grooves. The reasons for the abrupt stall at $\varphi=0.25$ in spite having essentially the same head coefficient as the open grooves are not clear at this point. We have also tested open grooves that have exits inclined at 20° to the z-axis in the positive circumferential direction with outlet ramps aligned with and against the flow direction (corresponding to negative and positive circumferential outflow directions). They both extend the stall margin to about $\varphi=0.19$, i.e., they are not as effective as the S groove. However, they do not cause an efficiency loss near BEP, and in fact reach a marginally higher peak efficiency of exceeding 0.85.

In view of the present findings, we have opted to focus our attention on the U and S grooves and study the differences between the flow fields that they generate. In the next section, we use the present non-transparent rings, to examine the flow structure in the rotor passage downstream of the grooves to determine their overall effects on blockage and flow direction. Studies planned for the future will examine the detailed flow structure within and around the grooves using transparent U and S grooves.
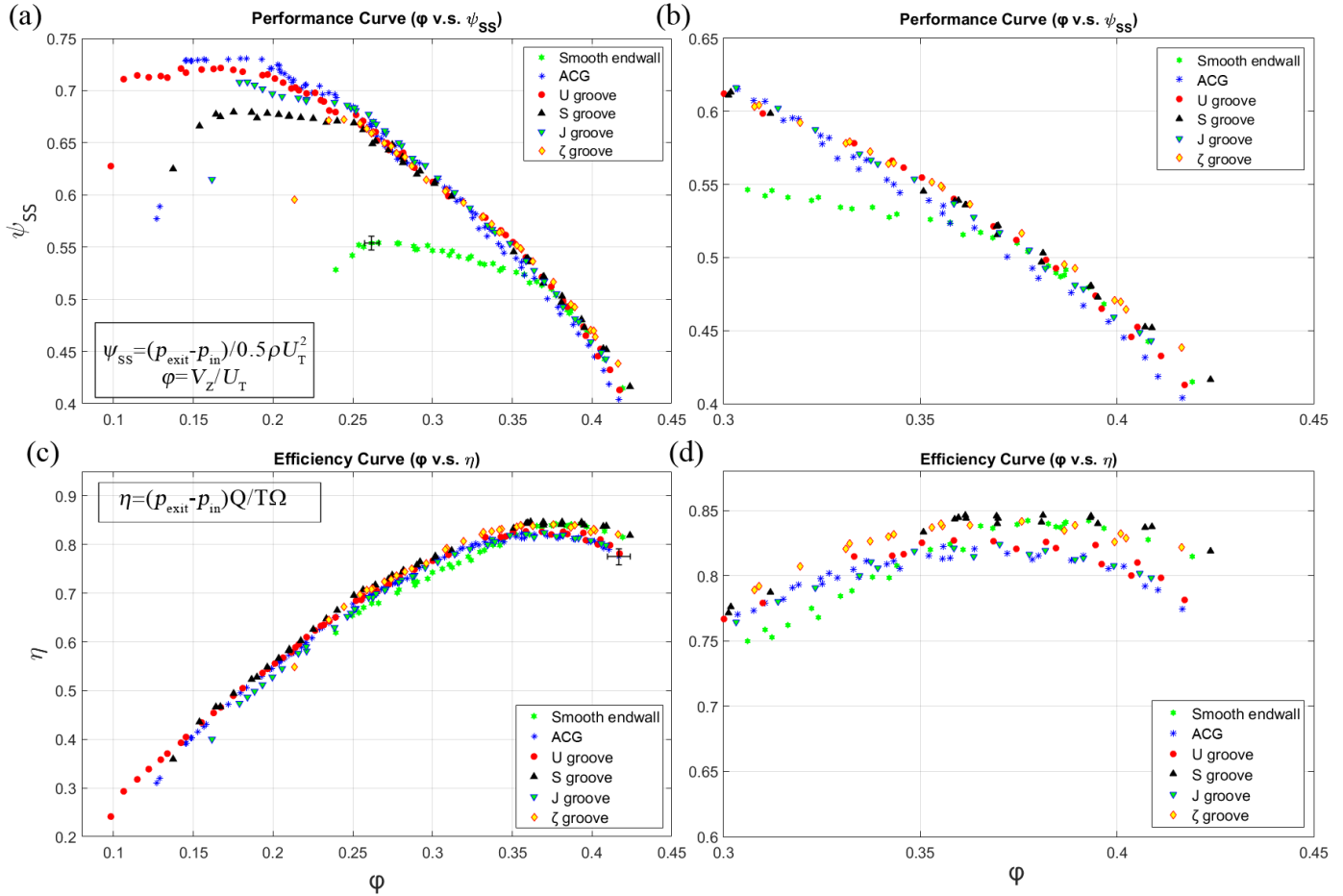
Figure 5: Comparisons of performance and efficiency curves for the different grooves to those of the smooth endwall: (a & b) static head rise, and (c & d) efficiency. (a & c) cover the entire flow rate range, and (b & d) focus on the vicinity of the BEP.

Flow Structure Downstream of the Grooves

Figure 6 shows the distributions of axial velocity scaled with V_Z covering an entire rotor passage for the U grooves (left column) and S grooves (right column). The top row shows the results for φ=0.25 (pre-stall for untreated groove), and the bottom row for φ=0.38 (BEP for untreated groove). The dashed lines show the location of U_Z/V_Z=1.0, red for the S grooves and black for the U grooves, above which the axial velocity falls below the mean values due to effects of tip blockage. The solid lines show the location of U_Z/V_Z=0.0, above which the axial velocity is negative, with the same color codes. Several trends are evident. First, at φ=0.25, the differences between velocity contour maps are small, but the U grooves create a wider region with negative U near the endwall casing. At φ=0.38, the U_Z/V_Z<1.0 and U_Z/V_Z<0 are noticeably wider for the U grooves, consistent with the corresponding reduced BEP efficiency. However, even in this case, the overall velocity distributions are not strikingly different.

Larger discrepancies occur in the distributions of U_θ/V_Z presented in Fig. 7. To accommodate comparisons to Fig. 6, each of the plots contains the lines indicating the locations of U_Z/V_Z=1.0 and 0.0. In all cases, the tip regions with 0<U_Z/V_Z

<1.0 are also characterized by high U_θ. At φ=0.25, U_θ for the S groove is higher than that of the U groove, and conversely, at φ=0.38, U_θ for the U groove is higher than that of the S groove. These trends suggest that reduced performance is associated with increased values of U_θ in the tip region. Interestingly, Houghton and Day [17] also observed an increase in U_θ and a minimal difference in axial velocity for circumferential grooves installed at mid-passage, which causes a higher efficiency penalty. They attribute the reduced efficiency to the elevated circumferential flow. In all cases, the U_Z/V_Z=1.0 line is located in a region with radial gradients in U_θ. Accordingly, the corresponding distributions of mean streamwise vorticity, presented in Fig. 8, show that for the most part peaks with positive values along or just above this line. A second thinner positive vorticity layer appears to form near the SS of the blade and seems to be connected to the SS below the tip corner. A third negative layer is evident primarily at φ=0.38 near the endwall close to the PS, just inboard of the U_Z/V_Z=0.0 line. At mid-passage, where this negative layer is located between the positive ones, it appears to have a kink. At φ=0.25, the negative layer is much thinner and remains confined very close to the endwall.
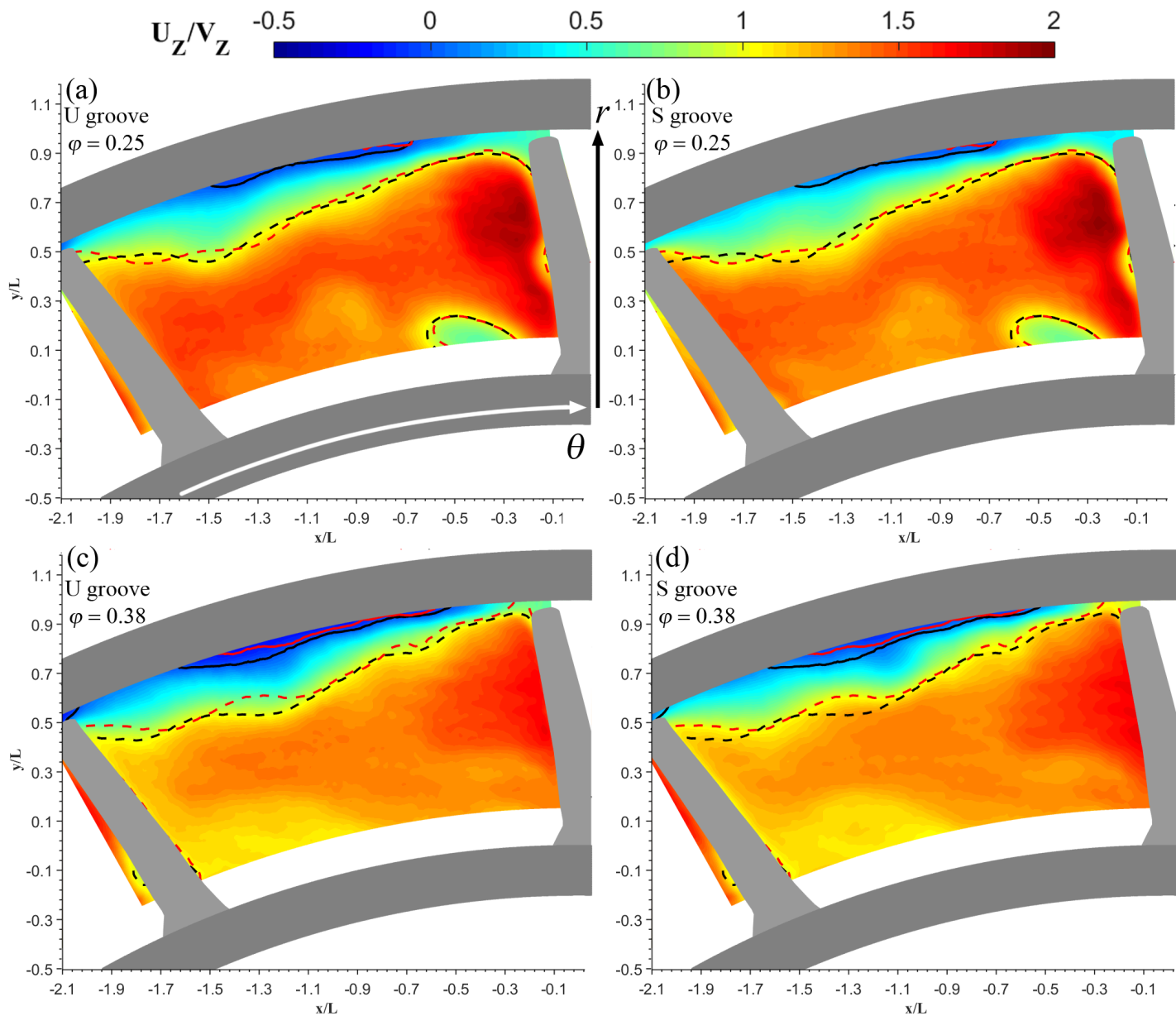
Figure 6: Distributions of axial velocity (U_Z/V_Z) in the (r, θ) plane located at $s/c = 0.86$. (a & b) $\varphi=0.25$; (c & d) $\varphi=0.38$. Left column (a &c) U groove; and right column (b &d) S groove; Dashed lines: $U_Z/V_Z=1$; solid lines: $U_Z/V_Z =0$. Black lines correspond to the U groove and red lines to the S groove.

In an attempt to understand the origin of the vorticity layers, Fig. 9 shows two sample cavitation images for an S groove at $\varphi=0.35$, which visualize the location of low-pressure regions, such as vortices. As discussed in previous publications [31], the cavitation is initiated after reducing the mean pressure in the facility. All the performance curves and velocity measurements are performed at higher pressures, without any cavitation. As is evident, in both cases, the main TLV is only slightly inclined to the circumferential direction, implying that its signature in the present PIV plane should appear as a broad low negative vorticity layer, mostly closer to the PS of the

blade. Velocity induced by this vortex above its center, i.e. near the endwall, is expected to be in the negative axial direction. These observations explain the presence of the $\langle\omega_Z\rangle<0$ layer and the region $U_Z/V_Z<0$ above it. The inner positive layer is associated with the backflow vortices [34], which, as discussed in the introduction, form at the interface between the region influenced by the tip leakage flow where U_θ is elevated, and the main passage flow inboard from it. The presence of these backflow vortices, which have a positive axial component, is evident from the cavitation images. For an untreated endwall, they are a primary contributor to the onset of rotating stall [34].

Finally, the outer/narrower $<\omega_Z> > 0$ layer develops along the inboard side of the tip leakage flow emerging from the tip gap carrying a series of vortex filaments, which are also evident from Fig. 9. The consistent presence of multiple layers with the same signs, confirming the present claims, is also demonstrated based on higher resolution measurements performed in the untreated machine [34].

In contrast, except for limited tip leakage cavitation just downstream of the ring, the cavitation image recorded at $\varphi=0.25$ with the S grooves do not show persistent organized large-scale structures developing downstream of the grooves. Hence, they are not presented. This observation indicates that at this flow rate, most of the TLV is ingested and scrambled by the grooves, in complete agreement with the observations and measurements performed using the transparent ACGs [38].

Hence, the corresponding axial vorticity distributions (Fig. 8) do not have a distinct negative vorticity layer propagating to the pressure side of the passage. The only place where the TLV has any noticeable effect is very close to the blade tip. As the flow rate increases and blade loading shifts downstream, a larger fraction of the vortex shedding and TLV rollup occurs downstream of the grooves, resulting in the patterns observed close to BEP. In summary, all the flow phenomena occurring in the tip region, including the elevated U_θ regions high are associated with tip leakage flows and their propagation away from the blade. Increased U_θ appears to correlate with reduced performance or efficiency. In addition, the U grooves generate a slightly wider region with reduced axial velocity, i.e. blockage, than the S grooves close to the best efficiency point.
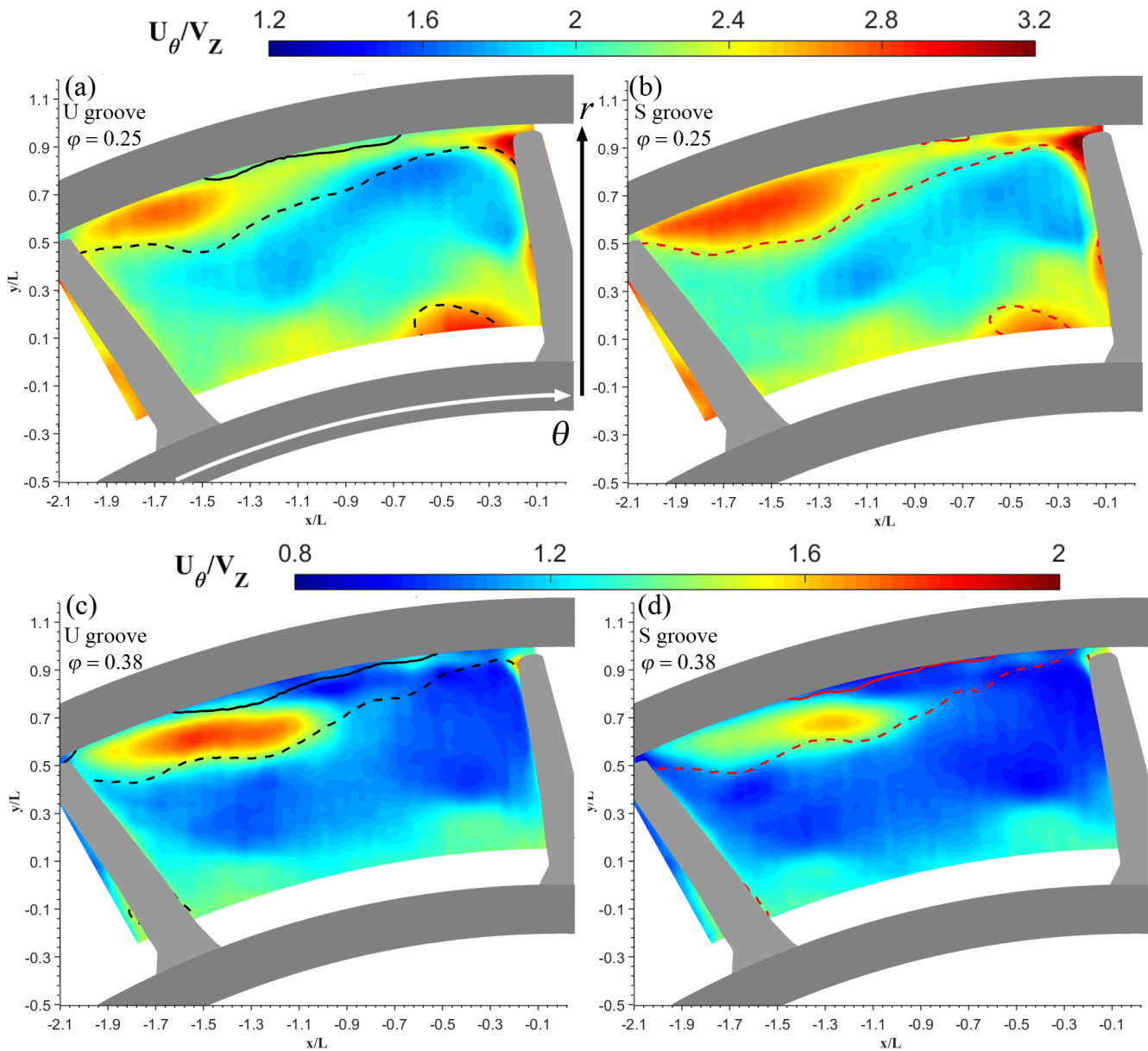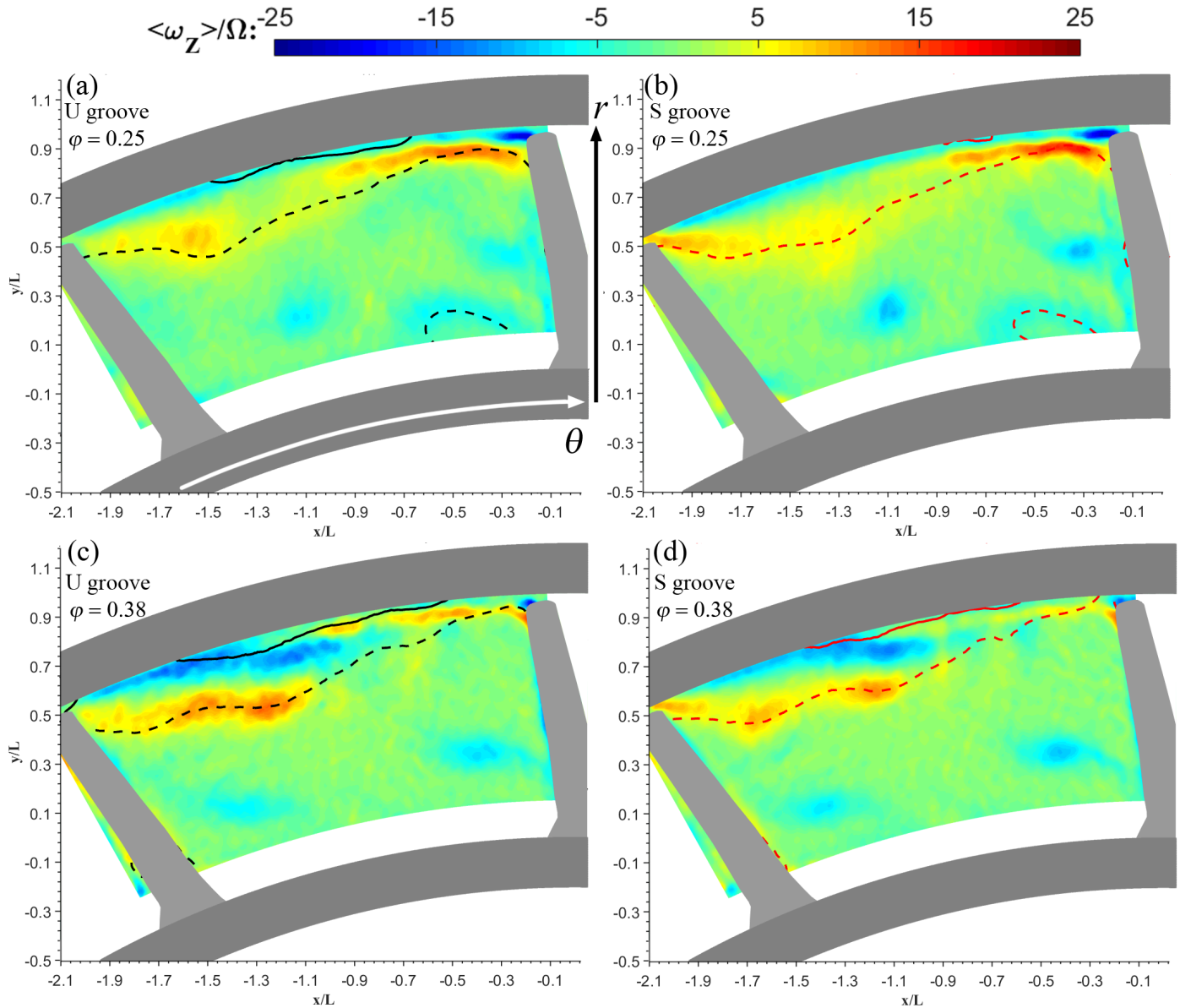

Figure 7: Distributions of circumferential velocity (U_θ/V_Z). For line definitions, see Fig. 6.

Figure 8: Distributions of axial vorticity ($<\omega_z>/\Omega$). Lines are defined in Fig. 6.

CONCLUSIONS

Prior velocity measurements and flow visualizations performed in the JHU refractive index matched facility have shown that axial casing grooves aimed at extending the stall margin have multiple effects on the flow structure. They ingest and scramble the TLV, prevent the formation of backflow vortices, which play a prominent role in the propagation of rotating stall, and cause substantial periodic variations in the flow angle around the rotor blade leading edge. To determine which of the co-occurring flow phenomenon is a key contributor to the suppression of stall, the present paper examines the impact of series of grooves, all with the same inlet (downstream end) geometry, but with outlets are aimed at different directions. Hence, the periodic suction of the TLV is expected to occur in all of them, but they would cause different periodic variations in flow angle near the blade LE.
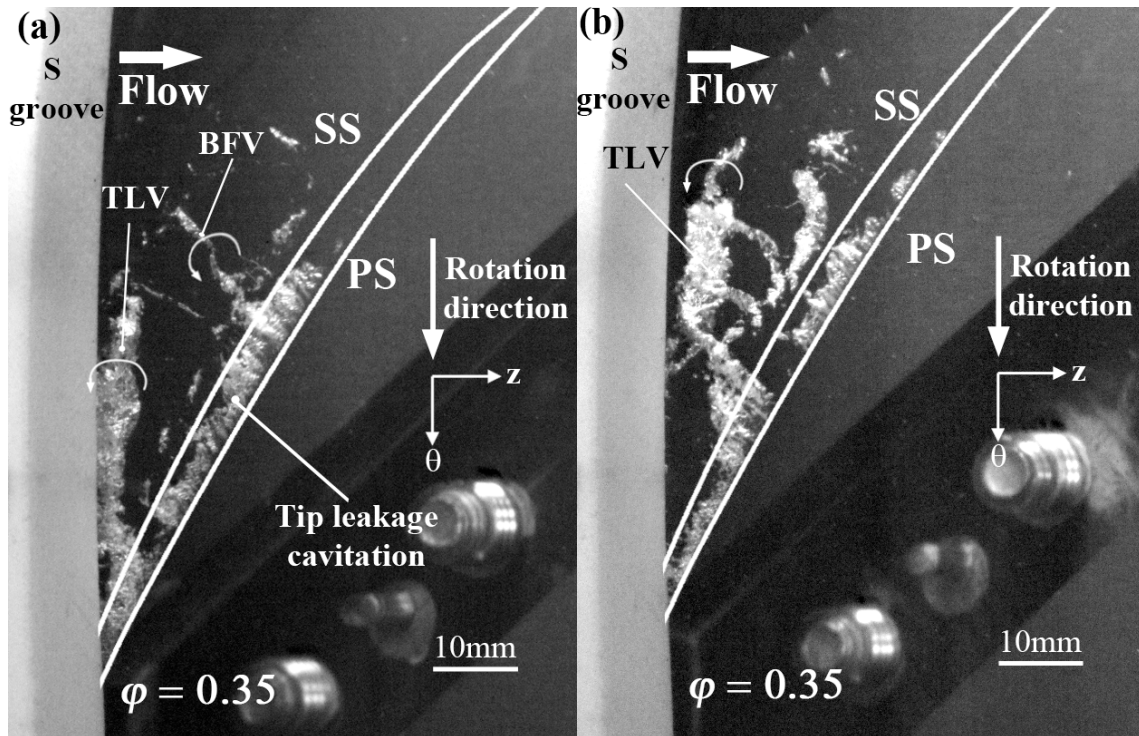
Figure 9: Sample cavitation images visualizing vortical structures in the tip region downstream of the S groove at $\varphi = 0.35$.

The U grooves that have exits aimed in the negative circumferential direction (against the blade rotation), similar to the original skewed semi-circular grooves, achieve the highest stall margin improvement of well above 60% but cause a 2.0% efficiency loss at near the best efficiency point. The S grooves, which have exits aimed at the positive circumferential direction, still achieve a substantial stall margin improvement of 36%, but not to the same extent as the U grooves. However, they do not reduce the efficiency at high flow rates compared to the untreated endwall. Several other grooves, which are aligned with and against the flow direction at the exit from the IGV, achieve lower stall margin improvements. These trends suggest that causing high periodic variations in flow angle around the blade leading edge, achieved by aiming the outflow from the groove against the direction of blade rotation, and achieves the highest stall margin improvement. However, this approach also involves a penalty of reduced maximum efficiency. In contrast, aiming the outflow with the blade rotation, which reduces the flow angle near the LE, appears to achieve a more moderate but still substantial improvement in stall margin, without the efficiency loss at high flow rates. Hence, of the geometries tested, the S grooves appear to have the best overall impact on the machine performance.

Due to the number of grooves involved, they have been manufactured with non-transparent materials using rapid prototyping. Hence, velocity measurements and flow visualizations have been limited to axial planes located downstream of the grooves, near the trailing edge of the rotor. The velocity measurements, which cover almost an entire blade passage, compare the flow structure downstream of the U and S grooves. In agreement with previously observed trends for circumferential grooves, reduced efficiency or performance co-occur with elevated circumferential velocity in the tip region. Blockage effects in the tip region occur downstream of both grooves, and the differences between them are subtle. Yet, near the best efficiency point, the regions with a negative axial velocity above the TLV, and where the axial velocity is lower than the spatially averaged value, are a little wider behind the U grooves. The vorticity profiles also suggest that at low flow rates the TLV is ingested almost entirely by the grooves, in contrast to the vicinity of the best efficiency point, where a considerable fraction of the TLV rollup occurs downstream of the grooves. To explain the present findings, the next series of experiments will focus on measuring and comparing the details of blade-groove interactions for the U and S grooves at varying flow rates using transparent, fully accessible flow near the blade leading edge.

NOMENCLATURE

A_T = through flow area
c = rotor blade tip chord
h = width of the rotor blade tip gap
H = rotor blade span
k = turbulent kinetic energy
L = nominal distance from the hub to the inner casing endwall
p_{exit} = static pressure at stator outlet
p_{in} = static pressure at IGV inlet
Q = volumetric flow rate
r, z, θ = radial, axial and circumferential coordinates
r^* = Normalized radial coordinate
s = rotor blade chordwise coordinate
T = motor input torque
u_r, u_z, u_θ = radial, axial and circumferential velocity
U_T = rotor blade tip speed
u' = velocity fluctuation
V_z = average axial velocity in the rotor passage
ρ = NaI solution density
φ = flow coefficient
θ_{blade} = Circumferential angle of a rotor passage
ψ_{SS} = static-to-static pressure rise coefficient
ω_θ = circumferential vorticity
Ω = rotor angular velocity
$< >$ = ensemble-averaged quantity

REFERENCES

[1]   Day, I. J., 1993, "Stall Inception in Axial Flow Compressors," J. Turbomach., **115**(1), pp. 1–9.

[2]   Hathaway, M. D., 2007, "Passive Endwall Treatments for Enhancing Stability," NASA Techincal Rep., **NASA/TM-20**.

[3]   Day, I. J., 2016, "Stall, Surge and 75 Years of Research," J. Turbomach., **138**(1), p. 011001.

[4]   Prince, D. C., Wisler, D. C., and Hilvers, D. E., 1975, "A Study of Casing Treatment Stall Margin Improvement Phenomena," Volume 1A: General, ASME, p. V01AT01A059.

[5]   Shabbir, A., and Adamczyk, J. J., 2005, "Flow Mechanism for Stall Margin Improvement due to Circumferential Casing Grooves on Axial Compressors," J. Turbomach., **127**(4), pp. 708–717.

[6]   Weichert, S., Day, I., and Freeman, C., 2011, "Self-Regulating Casing Treatment for Axial Compressor Stability Enhancement," Asme Turbo Expo, ASME, Vancouver, Canada, p. 13.

[7]   Prince D. C., J., Wisler, D. C., and Hilvers, D. E., 1975, "A Study of Casing Treatment Stall Margin improvement Phenomena," Trans ASME, pp. 75-GT-60.

[8]   Fujita, H., and Takata, H., 1984, "A Study on Configurations of Casing Treatment for Axial Flow Compressors," Bull. JSME, **27**(230), pp. 1675–1681.

[9]   Wilke, I., and Kau, H.-P., 2004, "A Numerical Investigation of the Flow Mechanisms in a High Pressure Compressor Front Stage With Axial Slots," J. Turbomach., **126**(3), pp. 339–349.

[10]   Smith, G. D. J., and Cumpsty, N. A., 1984, "Flow Phenomena in Compressor Casing Treatment," J. Eng. Gas Turbines Power, **106**(3), pp. 532–541.

[11]   Brandstetter, C., Kegalj, M., Wartzek, F., Heinichen, F., and Schiffer, H.-P., 2014, "Stereo PIV Measurement of Flow Structures underneath an Axial-Slot Casing Treatment on a One and a Half Stage Transonic Compressor," 17th International Symposium on Applications of Laser Techniques to Fluid Mechanics, Lisbon, Portugal, pp. 1–18.

[12]   Crook, A. J., Greitzer, E. M., Tan, C. S., and Adamczyk, J. J., 1993, "Numerical Simulation of Compressor Endwall and Casing Treatment Flow Phenomena," J. Turbomach., **115**(3), pp. 501–512.

[13]   Müller, M. W., Schiffer, H.-P., Voges, M., and Hah, C., 2011, "Investigation of Passage Flow Features in a Transonic Compressor Rotor," Proceedings of ASME Turbo Expo 2011: Power for Land, Sea and Air, Vancouver, Canada, pp. 1–11.

[14]   Osborn, W. M., Lewis, G. W. J., and Heidelberg, L. J., 1971, "Effect of Several Porous Casing Treatments on Stall Limit and on Overall Performance of an Axial-Flow Compressor Rotor," NASA Techincal Note, p. TN D-6537.

[15]   Seitz, P. A., 1999, "Casing Treatment for Axial Flow Compressors," University of Cambridge.

[16]   Beheshti, B. H., Teixeira, J. A., Ivey, P. C., Ghorbanian, K., and Farhanieh, B., 2004, "Parametric Study of Tip Clearance—Casing Treatment on Performance and Stability of a Transonic Axial Compressor," J. Turbomach., **126**(4), pp. 527–535.

[17]   Houghton, T., and Day, I., 2011, "Enhancing the Stability of Subsonic Compressors Using Casing Grooves," J. Turbomach., **133**(2), p. 021007.

[18]   Takata, H., and Tsukuda, Y., 1977, "Stall Margin Improvement by Casing Treatment --- Its Mechanism and Effectiveness," J. Eng. Power, **99**(1), pp. 121–133.

[19]   Johnson, M. C., and Greitzer, E. M., 1987, "Effects of Slotted Hub and Casing Treatments on Compressor Endwall Flow Fields," J. Turbomach., **109**(3), p. 380.

[20]   Pullan, G., Young, A. M., Day, I. J., Greitzer, E. M., and Spakovszky, Z. S., 2015, "Origins and Structure of Spike-Type Rotating Stall," J. Turbomach., **137**(5), p. 051007.

[21]   Hewkin-Smith, M., Pullan, G., Grimshaw, S. D., Greitzer, E. M., and Spakovszky, Z. S., 2017, "The Role of Tip Leakage Flow in Spike-Type Rotating Stall Inception," Volume 2D: Turbomachinery, ASME, p. V02DT46A009.

[22] Vo, H. D., Tan, C. S., and Greitzer, E. M., 2008, "Criteria for Spike Initiated Rotating Stall," J. Turbomach., **130**(1), p. 011023.

[23] Hoying, D. a., Tan, C. S., Vo, H. D., and Greitzer, E. M., 1999, "Role of Blade Passage Flow Structurs in Axial Compressor Rotating Stall Inception," J. Turbomach., **121**(4), pp. 735–742.

[24] Hah, C., Bergner, J., and Schiffer, H.-P., 2006, "Short Length-Scale Rotating Stall Inception in a Transonic Axial Compressor – Criteria and Mechanisms," Proceedings of ASME Turbo Expo 2006, pp. GT2006-90045.

[25] Inoue, M., Kuroumaru, M., Tanino, T., Nakamura, K., and Furukawa, M., 2000, "Behavior of Multiple Short Length-Scale Stall Cells Propagating in an Axial Compressor Rotor.," Trans. Japan Soc. Mech. Eng. Ser. B, **66**(January), pp. 804–809.

[26] Inoue, M., Kuroumaru, M., Yoshida, S., and Furukawa, M., 2002, "Short and Long Length-Scale Disturbances Leading to Rotating Stall in an Axial Compressor Stage With Different Stator/Rotor Gaps," J. Turbomach., **124**(3), pp. 376–384.

[27] Deppe, A., Saathoff, H., and Stark, U., 2005, "Spike-Type Stall Inception in Axial-Flow Compressors," Proceedings of the 6th European Conference on Turbomachinery, Lille, France, pp. 178–188.

[28] Yamada, K., Kikuta, H., Iwakiri, K., Furukawa, M., and Gunjishima, S., 2013, "An Explanation for Flow Features of Spike-Type Stall Inception in an Axial Compressor Rotor," J. Turbomach., **135**(2), p. 021023.

[29] Wu, H., Tan, D., Miorini, R. L., and Katz, J., 2011, "Three-Dimensional Flow Structures and Associated Turbulence in the Tip Region of a Waterjet Pump Rotor Blade," Exp. Fluids, **51**(6), pp. 1721–1737.

[30] Miorini, R. L., Wu, H., and Katz, J., 2012, "The Internal Structure of the Tip Leakage Vortex Within the Rotor of an Axial Waterjet Pump," J. Turbomach., **134**(3), p. 031018.

[31] Tan, D., Li, Y., Wilkes, I., Miorini, R., and Katz, J., 2015, "Visualization and Time-Resolved PIV Measurements of the Flow in the Tip Region of a Subsonic Compressor Rotor," J. Turbomach., **137**(4), p. 041007.

[32] Wu, H., Miorini, R. L., and Katz, J., 2011, "Measurements of the Tip Leakage Vortex Structures and Turbulence in the Meridional Plane of an Axial Water-Jet Pump," Exp. Fluids, **50**(4), pp. 989–1003.

[33] Wu, H., Miorini, R. L., Tan, D., and Katz, J., 2012, "Turbulence Within the Tip-Leakage Vortex of an Axial Waterjet Pump," AIAA J., **50**(11), pp. 2574–2587.

[34] Chen, H., Li, Y., Tan, D., and Katz, J., 2017, "Visualizations of Flow Structures in the Rotor Passage of an Axial Compressor at the Onset of Stall," J. Turbomach., **139**(4), p. 041008.

[35] Tan, D., Li, Y., Chen, H., Wilkes, I., and Katz, J., 2015, "The Three Dimensional Flow Structure and Turbulence in the Tip Region of an Axial Flow Compressor," ASME Turbo Expo 2015: Turbine Technical Conference and Exposition, pp. GT2015-43385.

[36] Li, Y., Chen, H., Tan, D., and Katz, J., 2016, "Effects of Tip Clearance and Operating Conditions on the Flow Structure and Reynolds Stresses within an Axial Compressor Rotor Passage," ASME Turbo Expo, pp. GT2016-57050.

[37] Chen, H., Li, Y., and Katz, J., 2018, "On the Interactions of a Rotor Blade Tip Flow With Axial Casing Grooves in an Axial Compressor Near the Best Efficiency Point," J. Turbomach., **141**(1), p. 011008.

[38] Chen, H., Li, Y., Koley, S. S., Doeller, N., and Katz, J., 2017, "An Experimental Study of Stall Suppression and Associated Changes to the Flow Structures in the Tip Region of an Axial Low Speed Fan Rotor by Axial Casing Grooves," J. Turbomach., **139**(12), p. 121010.

[39] Hah, C., 2017, "Effects of Double-Leakage Tip Clearance Flow on the Performance of a Compressor Stage With a Large Rotor Tip Gap," J. Turbomach., **139**(6), p. 061006.

[40] Wieneke, B., 2005, "Stereo-PIV Using Self-Calibration on Particle Images," Exp. Fluids, **39**(2), pp. 267–280.